

The effect of FeNi-AlN layer thickness on the response of magnetic SAW sensor by FEM simulation

Do Duy Phu^{1,2}, Hoang Si Hong¹, Le Van Vinh^{3,4}

¹School of Electrical and Electronic Engineering, Hanoi University of Science and Technology, Vietnam

²Hanoi University of Industrial, Hanoi, Vietnam

³Faculty of Computer Science, Phenikaa University, Hanoi, Vietnam

⁴Phenikaa Research and Technology Institute (PRATI), A&A Green Phoenix Group, Hoang Ngan, Trung Hoa, Cau Giay, Hanoi, Vietnam

Article Info

Article history:

Received May 24, 2023

Revised Sep 11, 2023

Accepted Oct 12, 2023

Keywords:

AlN

FeNi

Finite element method

Optimization structure

SAW-MO

Surface acoustic wave

ABSTRACT

In this study, we used simulation to investigate the optimal working point of a surface acoustic wave-magnetostriction sensor by varying the thickness of the magnetic sensitive layer using the finite elements method. We evaluated the sensor's sensitivity by simulating the responses at the optimal point and changing the thickness of the magnetic sensitive layer (h_3). Additionally, we reduced the piezoelectric substrate thickness (h_1) at the optimal point to determine the limit point of the center frequency (f_0) and improve the sensor sensitivity for low magnetic field intensity measurements by performing a wavelength reduction (λ). For the simulation, we selected a delay-line FeNi/IDT/AlN structure with specific materials and electrode parameters. Our results show that the optimal structure of the sensor is at $h_1=400 \mu\text{m}$, $\lambda=40 \mu\text{m}$, and $h_3=1,060 \text{ nm}$, with a maximum f_0 of 140.38493 MHz and maximum surface acoustic wave velocity of 5,615.4 m/s. At this optimal structure, the sensitivity reaches the maximum value of 10.287 kHz/Oe with a working range from 0 to 89 Oe. We also found that reducing the piezoelectric substrate thickness to 35 μm significantly reduces the manufacturing and simulation time, but the frequency response cannot determine the center frequency.

This is an open access article under the [CC BY-SA](https://creativecommons.org/licenses/by-sa/4.0/) license.



Corresponding Author:

Le Van Vinh

Phenikaa Research and Technology Institute (PRATI), A&A Green Phoenix Group

No. 167 Hoang Ngan, Trung Hoa, Cau Giay, Hanoi 11313, Vietnam

Email: vinh.levan@phenikaa-uni.edu.vn

1. INTRODUCTION

Surface acoustic wave (SAW) devices have numerous applications in the fields of actuators and sensors, including the microelectromechanical systems (MEMS) actuator [1]. SAW sensors have been applied in various fields, such as mechanical, biological, chemical, gas, and microfluidics, to measure physical quantities including temperature, pressure, viscosity, mass, stress, current, gas composition, magnetic field, and the spatial localization of partial discharges [2]–[9]. Recently, the wireless magnetic sensors with low energy consumption are essential for developments in the field of the internet of things, autonomous vehicles and the factory of the future. Common constructions for magnetic SAW sensors usually have a magnetic sensitive materials, an intermediate layers, an electrodes and a piezoelectric substrates (magnetic sensitive materials/intermediate layers/electrodes/piezoelectric substrates). Several recent studies indicate that common magnetostrictive sensitive materials, including Ni, FeGa, FeCo, and FeNi, have been combined with quartz and LiNbO₃ piezoelectric substrates to measure magnetic field intensity and current with high sensitivity [4]–[6], [10]–[17]. The results show that the thickness of the magnetic materials significantly

affect the sensitivity of the sensor [4], [11], [15]. Notely that the simulation approach was used to optimize the design parameters of sensors, in which the electromechanical equations set are solved numerically through finding boundary conditions to satisfy the CHRISTOFFEL equation and using perturbation theory [11]. In fact, it is difficult to determine the boundary conditions, and thus consequently this approach is not convenient to implement. Currently, the most popular simulation method for SAW sensors is using finite element method (FEM) through commercial software tools such as COMSOL and ANSYS. The survey shows that many studies have used FEM to simulate gas sensors, pressure sensors, magnetic field sensors, and SAW filters [6], [18]–[23]. Namely, the FEM with the COMSOL tool was used to evaluate the influence of the intermediate layer on the sensor properties of the magnetic SAW sensor [16].

Thus, in this work, we used the FEM with ANSYS software to simulate the SAW-MO sensor with FeNi/IDT/AIN structures. In this SAW-MO sensor, FeNi is selected because it has good sensitivity, low nonlinearity and small hysteresis; AIN is a piezoelectric material and has a large surface wave velocity that leads to being able to achieve the high sensitivity. The thickness of the FeNi and AIN layers changed during the simulation to determine the optimal parameters for the sensor structure to achieve the highest sensitivity.

The rest of the paper is organized as follows: section 2 presents the simulation process of the paper, which is divided into smaller sections, whereby section 2.1 explains the principle and structure parameters of the sensor, while section 2.2 gives mathematical model for FEM simulation, and section 2.3 presents FEM simulation process. Section 3 shows the results and discussions of this research paper and, finally, section 4 displays the conclusive findings for this research paper.

2. SIMULATION PROCESS

2.1. Principle and structure parameters of the sensor

Figure 1 illustrates the SAW-MO sensor structure. The sensor comprises an AIN piezoelectric substrate, which has two sets of electrodes, namely the input (IDT-in) and output (IDT-out) electrodes. These electrodes sandwich the FeNi sensitive layer (in a delay-line form). When a voltage is applied to the IDT-in, the piezoelectric substrate generates a surface acoustic wave through the reverse piezoelectric effect, which propagates through the FeNi sensitive layer to the IDT-out, where a forward piezoelectric effect occurs and forms a voltage on the IDT-out. The interaction between the measured magnetic field intensity (H) and the FeNi magnetic sensitive layer changes the frequency of this signal (or the SAW velocity). The structural parameters of the sensor are detailed in Figure 2 and Table 1. In the simulations, the sensor has a constant length (in the x_1 axis) and depth (in the x_3 axis), and initially, the sensor is simulated with $d = 10 \mu\text{m}$ (corresponding to the sensor with wavelength $\lambda = 40 \mu\text{m}$). The thickness of the piezoelectric substrate (h_1) is $400 \mu\text{m}$, while the thickness of the magnetic sensitive layer (h_3) varies to determine the optimal working point of the sensor. Subsequently, the simulation changes the thickness (h_1) of the piezoelectric layer to determine the limit of the sensor's working point when the wavelength λ is constant based on the found optimal point (h_3).

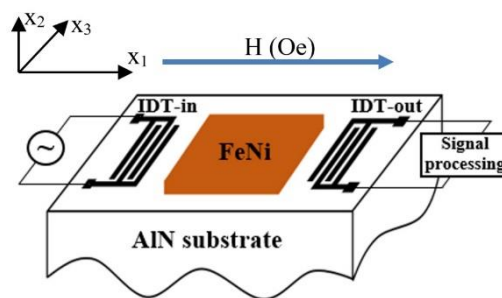


Figure 1. The SAW-MO sensor structure

2.2. Mathematical model for FEM simulation

In this work, we set up a mathematical model of the SAW-MO sensor in a piezoelectric material environment, representing the forward and reverse piezoelectric effects with a set of electromechanical (1) and (2) [24], [25].

$$T = cS - eE \quad (1)$$

$$D = e^T S + \varepsilon E \tag{2}$$

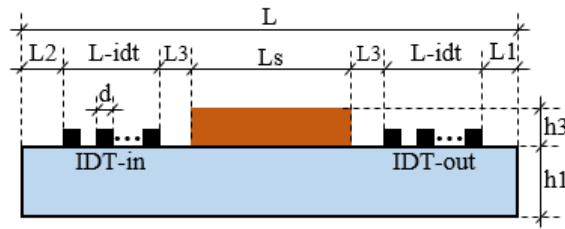


Figure 2. The SAW-MO sensor structure parameters

Table 1. Structural parameters of the sensor

Parameters	Symbol	Value (μm)
Number of IDT finger pair	n	25 pairs
Width of each finger	d	Vary
Left edge distance	$L2$	2,000
Right edge distance	$L1$	2,000
Length of IDT	$L - idt$	990
Length of magnetic sensitive layer	Ls	4,960
Thickness of piezoelectric layer	$h1$	Vary
Thickness of magnetic sensitive layer	$h3$	Vary
Gap between IDT and sensitive layer	$L3$	20
Sensor length	L	10,980

These equations involve parameters such as the elastic matrix (c), piezoelectric matrix (e), and dielectric constant matrix (ε) along with stress (T), strain (S), electric displacement (D), and electric field (E) (see in Table 2). We also use motion (3) and (4) [24] to describe particle movement in the solid, with phase velocity, particle displacement, and potential as variables.

$$\nabla \cdot T = \rho \frac{\partial^2 u}{\partial t^2} \tag{3}$$

$$E = -\nabla \Phi \tag{4}$$

Where u is the particle displacement in the solid, Φ is the potential, and ρ is the density of the piezoelectric material. Here the operators are:

$$\nabla = \left[\frac{\partial}{\partial x_1} \quad \frac{\partial}{\partial x_2} \quad \frac{\partial}{\partial x_3} \right] \tag{5}$$

$$\nabla \cdot = \begin{bmatrix} \frac{\partial}{\partial x_1} & 0 & 0 & 0 & \frac{\partial}{\partial x_3} & \frac{\partial}{\partial x_2} \\ 0 & \frac{\partial}{\partial x_2} & 0 & \frac{\partial}{\partial x_3} & 0 & \frac{\partial}{\partial x_1} \\ 0 & 0 & \frac{\partial}{\partial x_3} & \frac{\partial}{\partial x_2} & \frac{\partial}{\partial x_1} & 0 \end{bmatrix} \tag{6}$$

Combining (3) to (6) with (1), (2) and the condition $\nabla \cdot D = 0$, we can express the constitutive (7) in index form for the AlN piezoelectric material [4].

$$\begin{cases} \rho_A \frac{d^2 u_i^a}{dt^2} - C_{ijkl}^a \frac{d^2 u_k^a}{dx_l dx_j} - e_{kij} \frac{d^2 \phi}{dx_k dx_j} = 0 \\ e_{jkl} \frac{d^2 u_k^a}{dx_l dx_j} - \varepsilon_{jk} \frac{d^2 \phi}{dx_k dx_j} = 0 \end{cases} \tag{7}$$

This equation involves the density, elastic coefficient, piezoelectric coefficient, mechanical displacement, and electric field of AlN, as well as indices $i, j, k, l=1, 2, 3$. Similarly, we have the constitutive (8) for FeNi magnetic sensitive material, which does not involve electric or displacement components [4].

$$\rho_F \frac{d^2 u_i^F}{dt^2} - C_{ijkl}^F \frac{d^2 u_k^F}{dx_i dx_j} = 0 \quad (8)$$

The wave used in our study is the Rayleigh wave (V_R), and the velocity relationship between this wave and the shear wave (V_S) is described in (9) and (10) [26], [27], with anisotropy coefficient A and shear wave velocity V_S calculated differently for isotropic and anisotropic materials [24], [26].

$$\frac{V_R}{V_S} = \frac{0.436 + c_{12}/c_{11}}{0.5 + c_{12}/c_{11}} \quad (9)$$

$$\frac{V_R}{V_S} \approx \left[\frac{2}{A} \left(1 - \frac{c_{66}}{Ac_{11}} \right) \right]^{1/2} \quad (10)$$

We note that V_S is always greater than the surface acoustic wave velocity.

Table 2. Physical parameter set of AlN, Al, and FeNi materials [11], [28]–[30]

Material parameters		Value		
		AlN	Al	FeNi
Elastic stiffness coefficients (10^{11}N.m^{-2})	C_{11}	4.10		
	C_{12}	1.49		
	C_{13}	0.99		
	C_{33}	3.89		
	C_{44}	1.25		
	C_{66}	1.25		
Piezoelectric coefficients (C.m^{-2})	$e_{31} e_{33}$	0.58		
	e_{24}	1.55		
		0.48		
Dielectric constants	ϵ_{11}	9.0		
	ϵ_{22}	9.0		
	ϵ_{33}	9.0		
Density (kg.m^{-3})	ρ	3,300	2,697	8,380
Young's modulus (GPa)	E		70.3	E-H
Poison ratio	ν		0.345	0.3

Based on the sensor structure illustrated in Figure 2, the surface acoustic wave propagates through the delay-line element, which is coated with a magnetic sensitive layer made of FeNi with a variable thickness. Consequently, the surface acoustic wave experiences two factors. First, the mass (m) of the FeNi magnetic sensitive layer reduces the surface acoustic wave velocity [11], which can be calculated using (12). Second, the surface acoustic wave velocity gradually increases and approaches the shear velocity when the thickness of the FeNi sensitive layer increases [24], [26] or the AlN piezoelectric layer decreases. The mass is calculated as (11):

$$m = \rho_F \times (h3 \times Ls \times Ds) \quad (11)$$

In this simulation, the depth (Ds) and the length (Ls) of FeNi sensitive layer are constant, while its thickness ($h3$) varies, and its density (ρ_F) is defined as the constant $k = Ls \times Ds$. Therefore, the mass of the FeNi magnetic sensitive layer can be expressed using:

$$m = \rho_F \times k \times h3 \quad (12)$$

Moreover, the elastic coefficients of the FeNi magnetic sensitive material layer are determined by the relationship [11].

$$\begin{cases} C_{11}^F = \frac{E(1-\nu_F)}{(1+\nu_F)(1-2\nu_F)} \\ C_{12}^F = \frac{E\nu_F}{(1+\nu_F)(1-2\nu_F)} \\ C_{44}^F = \frac{E(1-2\nu_F)}{2(1+\nu_F)(1-2\nu_F)} \end{cases} \quad (13)$$

Where E is the Young's modulus defined by the E-H characteristic and the poisson coefficient (ν_F) is equal to 0.3. H is the measured magnetic field intensity.

To simulate the sensor's working response accurately, the E-H characteristic described in [11] is used to determine the sensor's working points. Specifically, as the measured magnetic field intensity (H) changes, it alters the young's modulus (E) of the magnetic sensitive material layer, which affects the propagation velocity of surface acoustic wave (V_R). Combining this with the relation $\Delta V_R/V_R = \Delta f/f_0$ [31], where f_0 is the center frequency of the sensor, determines the frequency change of the sensor. By varying the thickness (h_3) of the FeNi sensitive layer at $H = 0$ Oe, we can establish the relationship between the center frequency and the thickness of the FeNi sensitive layer to identify the optimal working point, which maximizes the acoustic wave velocity or resonant frequency at a given thickness. Subsequently, additional simulations are performed around the optimal working point to determine the sensor's working response and draw conclusions regarding the best sensitivity of the magnetic sensor. With the optimal working point fixed, the thickness of the AlN piezoelectric layer is varied to determine the central frequency limit point of the sensor with a constant wavelength. This serves as the basis for increasing the center frequency of the sensor, which hopefully enhances the sensitivity of the sensor when working at lower measuring ranges.

2.3. FEM simulation process

To simulate the sensor's working response, we used the constitutive (7) and (8) and data from Table 2. We performed FEM simulation in the following steps: firstly, entering the physical parameters (Table 2) and declaring the structure parameters (Table 1); secondly, building the sensor structure (as shown in Figure 2), meshing and changing material layers; thirdly, applying voltage to the IDT-in and setting boundary conditions; finally, solving and reading results. The simulation process is illustrated in Figure 3.

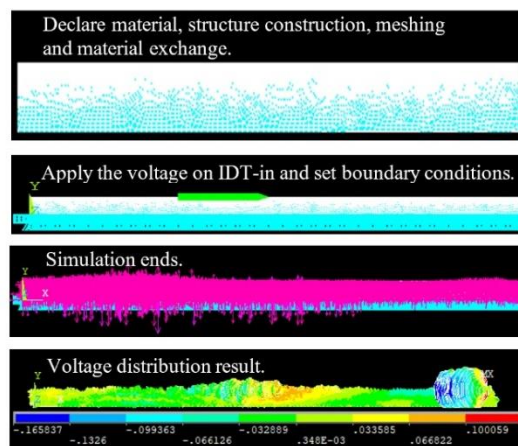


Figure 3. FEM simulation process images

We ensured accuracy while improving simulation speed by meshing the sensor with thicker meshing density at the top where the IDTs and magnetic sensitive layer FeNi are located and thinner density at the bottom. With a meshing step of about $\lambda/40 = 1 \mu\text{m}$, the model had around 113,556 elements, ensuring convergent results. The boundary conditions were set as follows: the top surface had a free mechanical condition and zero voltage, the bottom had a fixed mechanical condition and grounding voltage, and the junction between two materials had free mechanical conditions and continuous voltage. All side edges of the sensor had free conditions.

We applied a square pulse voltage of 100 V and pulse width of 10 ns to the IDT-in, then let the FEM calculation run long enough for the surface acoustic wave to propagate from IDT-in to IDT-out (about 1,500 ns), with a signal sampling period of 0.3 ns to satisfy Shannon's theorem. The output voltage was read on the IDT-out in the time domain and converted to the frequency domain using the FFT spectral density transform algorithm to determine the resonant frequency (f_c) and surface acoustic wave velocity. We iteratively repeated this process to find the optimal working point by changing the FeNi sensitive layer thickness and to determine the working responses around the optimal point as the measured magnetic field intensity (H) changes. We also changed the AlN piezoelectric layer thickness to determine the limit point of the center frequency and the sensor's working response when the center frequency is increased, with the aim of improving the sensor's sensitivity when measuring at a lower range.

3. RESULTS AND DISCUSSION

The simulation results presented in Table 3, Figures 4 and 5 reveal a two-stage behavior in the characteristic. In the first stage, increasing the thickness of the FeNi magnetic sensitive layer up to 1,060 nm results in an increase in the center frequency and surface acoustic wave velocity. However, in the second stage, further increases in the thickness of the FeNi layer lead to a decrease in the center frequency and surface acoustic wave velocity. These results are consistent with the theoretical framework proposed in this study and corroborated by previous research [4], [11], [15].

Table 3. Center frequency (f_0) and surface acoustic wave velocity (V_R) at the different thickness points of the FeNi magnetic sensitive layer (h_3), $V_R = \lambda \times f_0$, $h_1 = 400 \mu\text{m}$ and $\lambda = 40 \mu\text{m}$

h_3 (nm)	f_0 (Hz)	V_R (m/s)
340	139,518,230	5,580.7
420	139,587,400	5,583.5
580	139,766,440	5,590.7
660	139,933,270	5,597.3
760	140,051,270	5,602.1
820	140,157,060	5,606.3
920	140,238,440	5,609.5
1,000	140,303,550	5,612.1
1,060	140,384,930	5,615.4
1,140	140,319,820	5,612.8
1,210	140,177,410	5,607.1
1,280	139,672,850	5,586.9
1,340	139,229,330	5,569.2

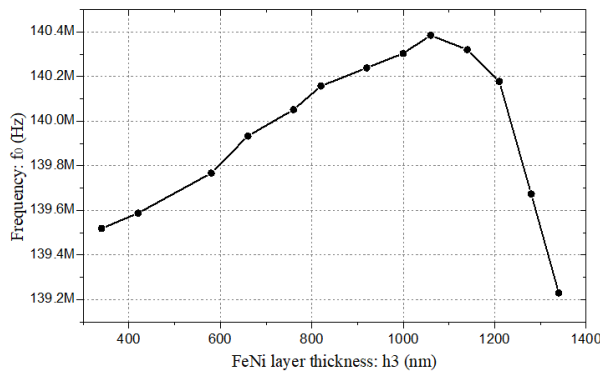


Figure 4. Relationship between the f_0 and FeNi layer thickness (h_3) at $H = 0$ Oe

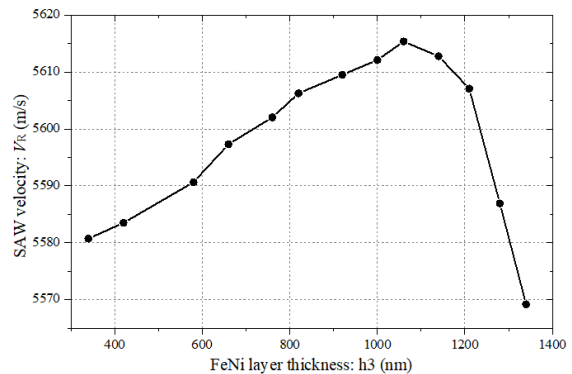


Figure 5. Relationship between the V_R and FeNi layer thickness (h_3) at $H = 0$ Oe

Based on the simulation results, we identify the optimal working point of the sensor at $h_3 = 1,060$ nm, when $h_1 = 400 \mu\text{m}$ and $\lambda = 40 \mu\text{m}$ remain unchanged. This conclusion follows from the fact that the center frequency and surface acoustic wave velocity reach their maximum values at this thickness. To gain a clearer understanding of the process used to determine the center frequency of the sensor at different thicknesses (h_3) of the FeNi magnetic sensitive layer, Figure 6 displays the frequency response of the sensor at three thickness points: 1,000 nm, 1,060 nm, and 1,210 nm. We determine the center frequency of the sensor for each thickness point by identifying the resonance peak of the frequency response.

We simulated the sensor's working response at different FeNi magnetic sensitive layer thicknesses, including 1,000 nm, 1,060 nm, and 1,210 nm, around the optimal working point. The simulation results are presented in Figure 7 and Tables 4 to 6. At $h_3 = 1,000$ nm, the sensor's response range is $H = [0 \div 109]$ Oe, with corresponding output frequencies of $f = [140.30355 \div 139.35954]$ MHz, or frequency shift $\Delta f = [0 \div -944.01]$ kHz. The sensor has a center frequency of $f_0 = 140.30355$ MHz when $H = 0$ Oe. Similarly, at $h_3 = 1,060$ nm, the sensor's response range is $H = [0 \div 89.0]$ Oe, with corresponding output frequencies of $f = [140.38493 \div 139.4694]$ MHz, or frequency shift $\Delta f = [0 \div -915.53]$ kHz. The sensor has a center frequency of $f_0 = 140.38493$ MHz when $H = 0$ Oe. At $h_3 = 1,210$ nm, the sensor's response range is $H = [0 \div 112.0]$ Oe, with corresponding output frequencies of $f = [140.17741 \div 139.12269]$ MHz, or frequency shift $\Delta f = [0 \div -105.472]$ kHz. The sensor has a center frequency of $f_0 = 140.17741$ MHz when $H = 0$ Oe.

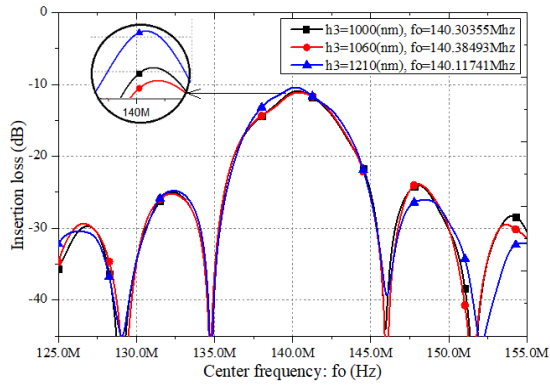


Figure 6. Frequency response around the sensor's optimum working point

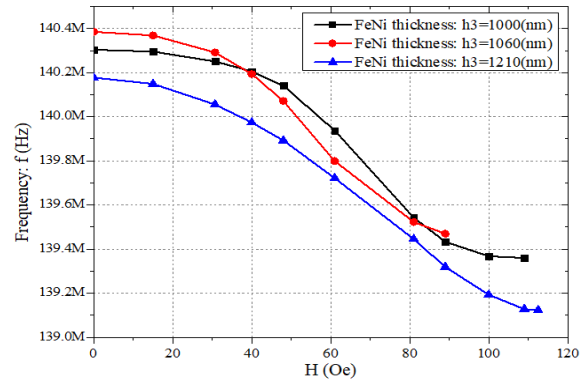


Figure 7. Working response of the sensor at the different thickness of FeNi magnetic sensitive layer

Table 4. Frequency response (f) and frequency shift (Δf) to measured magnetic field intensity (H) of the sensor at $h3 = 1,000$ nm, $h1 = 400 \mu\text{m}$ and $\lambda = 40 \mu\text{m}$

H (Oe)	f (Hz)	Δf (Hz)
0.0	140,303,550	0
15.0	140,295,410	-8,140
30.7	140,250,650	-52,900
40.0	140,205,890	-97,660
48.0	140,140,790	-162,760
61.0	139,937,340	-366,210
81.0	139,542,640	-760,910
89.0	139,432,780	-870,770
100.0	139,367,680	-935,870
109.0	139,359,540	-944,010

Table 5. Frequency response (f) and frequency shift (Δf) to measured magnetic field intensity (H) of the sensor at $h3 = 1,060$ nm, $h1 = 400 \mu\text{m}$ and $\lambda = 40 \mu\text{m}$

H (Oe)	f (Hz)	Δf (Hz)
0.0	140,384,930	0
15.0	140,368,650	-16,280
30.7	140,291,340	-93,590
40.0	140,193,680	-191,250
48.0	140,071,610	-313,320
61.0	139,798,990	-585,940
81.0	139,522,300	-862,630
89.0	139,469,400	-915,530

Table 6. Frequency response (f) and frequency shift (Δf) to measured magnetic field intensity (H) of the sensor at $h3 = 1,210$ nm, $h1 = 400 \mu\text{m}$, and $\lambda = 40 \mu\text{m}$

H (Oe)	f (Hz)	Δf (Hz)
0.0	140,177,410	0
15.0	140,148,930	-28,480
30.7	140,055,340	-122,070
40.0	139,973,960	-203,450
48.0	139,892,580	-284,830
61.0	139,721,680	-455,730
81.0	139,444,990	-732,420
89.0	139,318,850	-858,560
100.0	139,192,710	-984,700
109.0	139,127,600	-1,049,810
112.5	139,122,690	-1,054,720

We determined the sensor's sensitivity in two cases based on its working responses at different $h3$ points. In the first case, the sensitivity is calculated over the full response scale of the sensor. At $h3 = 1,000$ nm, the response range $H = [0 \div 109]$ Oe, with an achieved sensitivity S_n of 8.661 kHz/Oe; at $h3 = 1,060$ nm, the response range $H = [0 \div 89]$ Oe, with an achieved sensitivity S_n of 10.287 kHz/Oe; and at $h3 = 1,210$ nm,

the response range $H = [0 \div 112.5]$ Oe, with an achieved sensitivity S_n of 9.375 kHz/Oe. The details are presented in Table 7 and Figure 8. In the second case, the sensitivity is calculated on the same response scale of the sensor $H = [0 \div 89]$ Oe. At $h_3 = 1,000$ nm, the achieved sensitivity S_n is 8.661 kHz/Oe; at $h_3 = 1,060$ nm, the achieved sensitivity S_n is 10.287 kHz/Oe; and at $h_3 = 1,210$ nm, the achieved sensitivity S_n is 9.375 kHz/Oe.

Table 7. The sensitivity (S_n) of sensor at points h_3 when $\lambda = 40 \mu\text{m}$ and $h_1 = 400 \mu\text{m}$

The full scale		The same scale $H = [0 \div 89]$ Oe	
h_3 (nm)	S_n (kHz/Oe)	h_3 (nm)	S_n (kHz/Oe)
0	0	0	0
1,000	8.661	1,000	9.784
1,060	10.287	1,060	10.287
1,210	9.375	1,210	9.647

In the second case, the sensitivity of the sensor is calculated on the same response scale of the sensor $H = [0 \div 89]$ (Oe), with achieved sensitivities of 8.661 kHz/Oe at $h_3 = 1,000$ nm, 10.287 kHz/Oe at $h_3 = 1,060$ nm, and 9.375 kHz/Oe at $h_3 = 1,210$ nm. Details are shown in Table 7 and Figure 9. These results indicate that at $h_3 = 1,060$ nm, the sensor exhibits the highest surface acoustic wave velocity and center frequency, resulting in the maximum sensitivity of 10.287 kHz/Oe in both cases. Our findings are in line with previous research in [6], which shows that higher surface acoustic wave velocity or center frequency leads to greater sensitivity. Additionally, to identify the points on the response range of the sensor when the magnetic field intensity changes from 0 to 89 Oe, we examined the resonance peaks on the frequency responses, as shown in Figures 10 to 12.

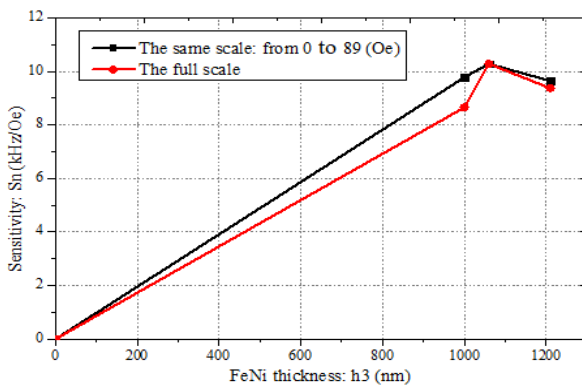


Figure 8. Relationship between the sensitivity and thickness (h_3) of FeNi magnetic sensitive layer

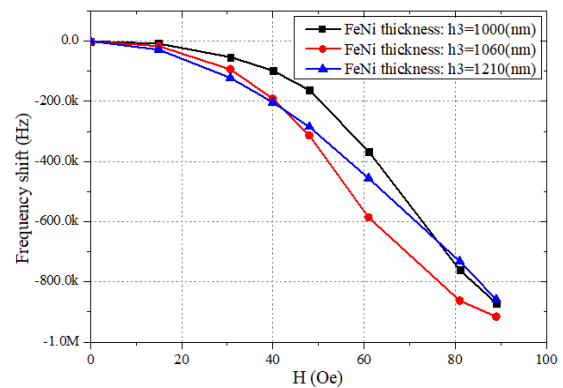


Figure 9. Frequency shift response of FeNi/IDT/AIN sensor with the same response scale

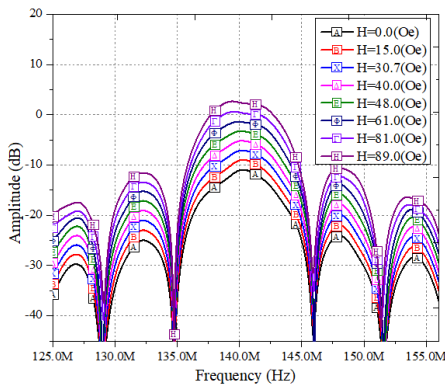


Figure 10. Frequency response of FeNi/IDT/AIN sensor at $h_3 = 1,000$ nm

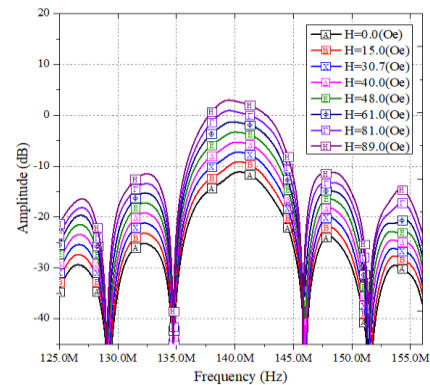


Figure 11. Frequency response of FeNi/IDT/AIN sensor at $h_3 = 1,060$ nm

We conducted simulations to investigate the influence of piezoelectric substrate thickness on the central frequency limit of the sensor. The results indicate that decreasing the piezoelectric substrate thickness increases the center frequency, as shown in Figures 13 and 14. This finding is consistent with previous studies in [6], [24], [26], [27], which suggest that as the piezoelectric substrate thickness decreases, the surface acoustic wave velocity approaches the shear wave velocity.

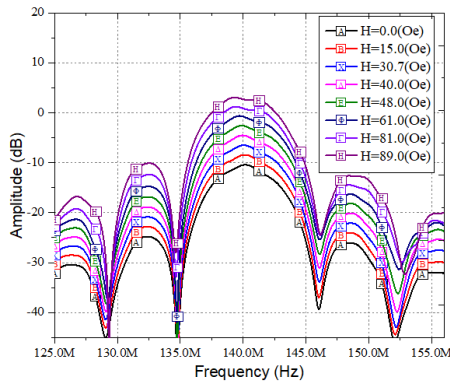


Figure 12. Frequency response of FeNi/IDT/AIN sensor at $h_3 = 1,210$ nm

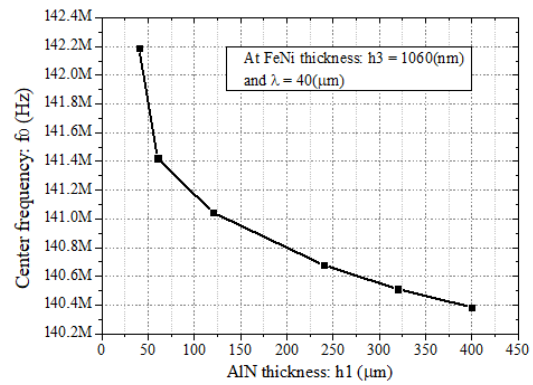


Figure 13. Center frequency response with varying h_1 at $h_3 = 1,060$ nm and $\lambda = 40$ μ m

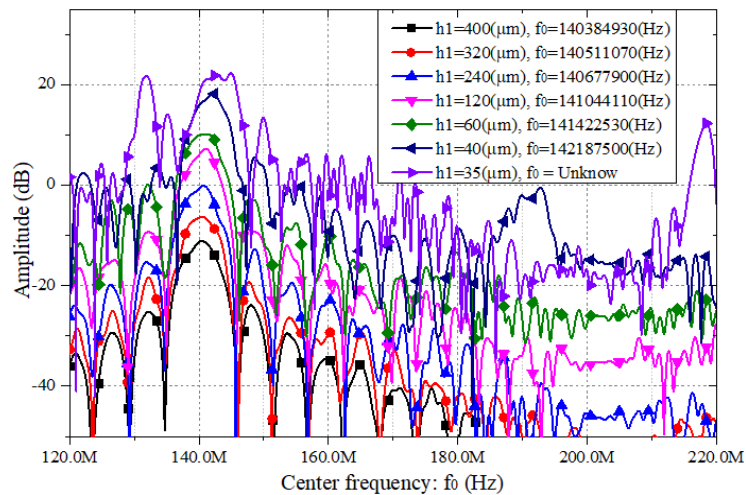


Figure 14. Frequency response of the sensor at h_1 with keeping $h_3 = 1,060$ nm and $\lambda = 40$ μ m

However, when the piezoelectric substrate thickness is reduced to less than one wavelength (see in Figure 14), the frequency characteristic at $h_1 = 35$ μ m no longer exhibits a resonance peak, leading to the indeterminability of the center frequency, unlike points with greater thickness. This phenomenon can be explained by the fact that when voltage is applied to the IDT-in, the piezoelectric material undergoes deformation due to the reverse piezoelectric effect from the surface to a depth of approximately one wavelength (λ), as stated in [26]. Thus, if the piezoelectric substrate thickness is greater than approximately one wavelength, the deformation region on the piezoelectric substrate is preserved. However, if the thickness is less than one wavelength, the deformation region is not preserved, causing the surface acoustic wave to be cut off at the lower peak, and as a result, the frequency characteristics are not preserved.

To preserve the frequency characteristics of the sensor, we can reduce the wavelength to $\lambda = 30$ μ m or increase the center frequency. The simulation results, which are shown in Figure 15, demonstrate that the frequency center $f_0 = 218.46517$ MHz when the wavelength is reduced to $\lambda = 30$ μ m. The working range of the sensor is $[0 \div 89]$ Oe, as shown in Figure 10, and the highest sensitivity is achieved when the magnetic sensitive layer thickness h_3 is 1,060 nm. However, the sensitivity is lower in the segment from 0 to 35 Oe, as seen from the frequency shift characteristic of the sensor at $h_3 = 1,060$ nm. To increase the

sensitivity of this segment, we can reduce the piezoelectric substrate thickness, which also reduces the fabrication and simulation time, and increase the center frequency of the sensor. The response simulation results of the sensor are shown in Figure 16. The simulation results show that the center frequency $f_0 = 218.46517$ MHz, the working range reaches from 0 to 33.1 Oe with the frequency shift of 248.21 kHz when the sensor has the parameters $h1 = 35 \mu\text{m}$, $\lambda = 30 \mu\text{m}$, and $h3 = 1,060$ nm. On the other hand, the structure of the sensor with the parameters $h1 = 400 \mu\text{m}$, $\lambda = 40 \mu\text{m}$, and $h3 = 1,060$ nm only gives the frequency shift of 118.79 kHz when considering the working range from 0 to 33.1 Oe. These results demonstrate that increasing the center frequency increases the sensitivity of the sensor, as shown in Table 8.

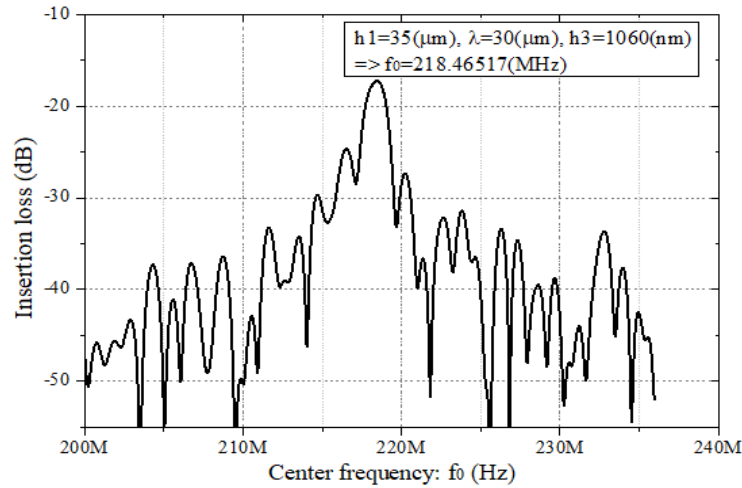


Figure 15. Frequency response of the sensor when $h1 = 35 \mu\text{m}$, $\lambda = 30 \mu\text{m}$, $h3 = 1,060$ nm

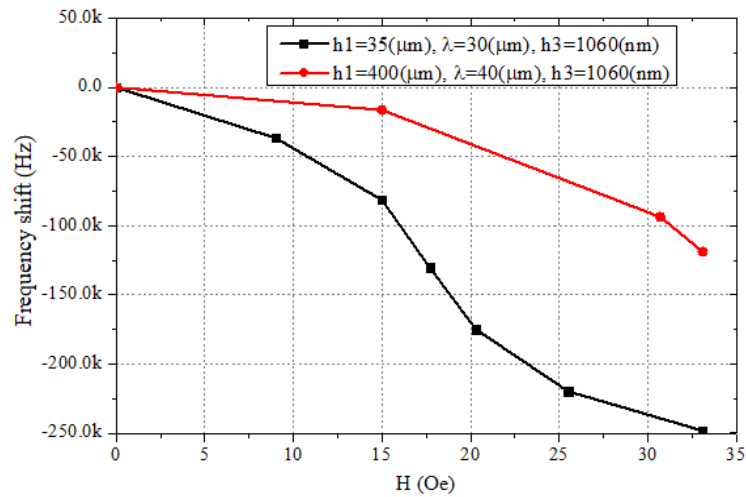


Figure 16. Frequency shift response of sensor at $h3 = 1,060$ nm

Table 8. The S_n and Δf of two structures with working range from 0 to 33.1 Oe

Structure parameters			Δf (kHz)	S_n (kHz/Oe)
$h1$ (μm)	λ (μm)	$h3$ (nm)		
400	40	1,060	118.79	3.589
35	30	1,060	248.21	7.499

Obviously, in this research, we have optimized the design parameters of the FeNi/IDT/AlN sensor structure with the sensitivity of 10.287 kHz/Oe which increases ~1.183 times compared to the sensitivity (8.698 kHz/Oe) of the FeNi/IDT/AlN sensor structure and ~4.387 times compared to the sensitivity (2.345 kHz/Oe) of the FeNi/IDT/LiNbO₃ sensor structure in previous work [6]. This increasing sensitivity is significant and indicates that it is necessary to perform simulations to optimize the sensor parameters.

4. CONCLUSION

In this paper, we used finite element method simulations to investigate the SAW-MO sensor with a FeNi/IDT/AlN structure. Firstly, we explored the optimal thickness (h_3) of the FeNi magnetic sensitive layer to achieve the best sensor performance. Next, we examined the impact of the magnetic sensitive layer thickness on the sensor's sensitivity. We also considered the influence of the AlN piezoelectric substrate thickness on the sensor's center frequency. Our results demonstrate that the optimal structure of the sensor is achieved at $h_3 = 1,060$ nm, with a highest surface acoustic wave velocity of 5,615.4 m/s and a highest center frequency of 140.38493 MHz. We observed that the sensitivity of the sensor reaches its maximum value of 10.287 kHz/Oe at $h_3 = 1,060$ nm. Additionally, we found that reducing the thickness of the AlN piezoelectric substrate to $h_1 = 35$ μm at the optimal point $h_3 = 1,060$ nm resulted in an increased sensitivity of 7.499 kHz/Oe and a working range from 0 to 33.1 Oe. In comparison, the sensitivity of the sensor structure with $h_1 = 400$ μm , $\lambda = 40$ μm , and $h_3 = 1,060$ nm was only 3.589 kHz/Oe within the same working range. In the future, the effect of the surface morphology of magnetic sensitive layer on the sensor's sensitivity will be conducted and experiments will be performed.




REFERENCES

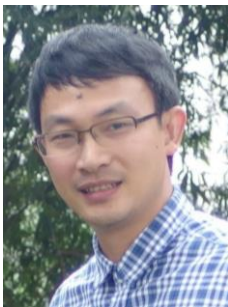
- [1] D. Mandal and S. Banerjee, "Surface Acoustic Wave (SAW) Sensors: Physics, Materials, and Applications," *Sensors*, vol. 22, no. 3, Jan. 2022, doi: 10.3390/s22030820.
- [2] S. Beeby, E. Graham, K. Michael, and W. Neil, *MEMS mechanical sensors*. Boston, London: Artech House, 2004.
- [3] T.-R. Hsu, *MEMS and microsystems: design, manufacture, and nanoscale engineering*. John Wiley & Sons, 2008.
- [4] Y. Sun, Y. Jia, Y. Zhang, L. Cheng, Y. Liang, and W. Wang, "Enhanced Sensitivity of FeGa Thin-Film Coated SAW Current Sensor," *Applied Sciences*, vol. 11, no. 24, Dec. 2021, doi: 10.3390/app112411726.
- [5] N. H. Ha, N. H. Nam, D. D. Dung, N. H. Phuong, P. D. Thach, and H. S. Hong, "Hydrogen Gas Sensing Using Palladium-Graphene Nanocomposite Material Based on Surface Acoustic Wave," *Journal of Nanomaterials*, vol. 2017, pp. 1–6, 2017, doi: 10.1155/2017/9057250.
- [6] D. P. Do, S. H. Hoang, and V. V. Le, "Simulating the piezoelectric substrate influence on the characteristics of surface acoustic wave-magnetostriction sensor based on the FeNi magnetic sensitive material," *Science & Technology Development Journal - Engineering and Technology*, 2022, doi: 10.32508/stdjet.v5i2.945.
- [7] A. Pohl, R. Steindl, and L. Reindl, "The 'intelligent tire' utilizing passive SAW sensors measurement of tire friction," *IEEE Transactions on Instrumentation and Measurement*, vol. 48, no. 6, pp. 1041–1046, 1999, doi: 10.1109/19.816111.
- [8] M. I. F. M. Radzi *et al.*, "Development process and testing of partial discharge detection device on medium voltage XLPE cable," *Indonesian Journal of Electrical Engineering and Computer Science*, vol. 19, no. 3, Sep. 2020, doi: 10.11591/ijeecs.v19.i3.pp1297-1305.
- [9] B. Danouj, S. A. Tahan, E. David, and M. Lotfi, "Partial discharges location in power transformers using piezoceramic sensors," *International Journal of Electrical and Computer Engineering (IJECE)*, vol. 11, no. 3, Jun. 2021, doi: 10.11591/ijece.v11i3.pp1942-1950.
- [10] W. Wang, Y. Jia, X. Liu, and S. He, "Development of a novel SAW current sensor based on the magnetostrictive effect," in *2015 IEEE International Ultrasonics Symposium, IUS 2015*, IEEE, Oct. 2015, pp. 1–3, doi: 10.1109/ULTSYM.2015.0354.
- [11] J. Tong *et al.*, "Development of a magnetostrictive FeNi coated surface acoustic wave current sensor," *Applied Sciences (Switzerland)*, vol. 7, no. 8, Jul. 2017, doi: 10.3390/app7080755.
- [12] J. Labrenz *et al.*, "Frequency Response of SAW Delay Line Magnetic Field/Current Sensor," *IEEE Sensors Letters*, vol. 3, no. 10, pp. 1–4, Oct. 2019, doi: 10.1109/LSSENS.2019.2943129.
- [13] F. Muhammad, H. Hong, P. Zhang, and Q. Abbas, "Measurement of magnetic field components using a single passive SAW magnetic sensor," *Sensors and Actuators A: Physical*, vol. 352, Apr. 2023, doi: 10.1016/j.sna.2023.114163.
- [14] V. Schell *et al.*, "Magnetic anisotropy controlled FeCoSiB thin films for surface acoustic wave magnetic field sensors," *Applied Physics Letters*, vol. 116, no. 7, Feb. 2020, doi: 10.1063/1.5140562.
- [15] W. Wang, Y. Jia, X. Liu, Y. Liang, X. Xue, and Z. Du, "Enhanced sensitivity of temperature-compensated SAW-based current sensor using the magnetostrictive effect," *Smart Materials and Structures*, vol. 26, no. 2, Feb. 2017, doi: 10.1088/1361-665X/aa5137.
- [16] M. Elhosni, O. Elmazria, A. Talbi, K. A. Aissa, L. Bouvot, and F. Sarry, "FEM Modeling of Multilayer Piezo-magnetic Structure Based Surface Acoustic Wave Devices for Magnetic Sensor," *Procedia Engineering*, vol. 87, pp. 408–411, 2014, doi: 10.1016/j.proeng.2014.11.276.
- [17] M. Kadota and S. Ito, "Sensitivity of Surface Acoustic Wave Magnetic Sensors Composed of Various Ni Electrode Structures," *Japanese Journal of Applied Physics*, vol. 51, no. 7S, Jul. 2012, doi: 10.1143/JJAP.51.07GC21.
- [18] M. Elhosni *et al.*, "Magnetic field SAW sensors based on magnetostrictive-piezoelectric layered structures: FEM modeling and experimental validation," *Sensors and Actuators A: Physical*, vol. 240, pp. 41–49, Apr. 2016, doi: 10.1016/j.sna.2015.10.031.
- [19] V. Kutiš, G. Gálík, V. Královič, I. Rýger, E. Mojto, and T. Lalinský, "Modelling and Simulation of SAW Sensor Using FEM," *Procedia Engineering*, vol. 48, pp. 332–337, 2012, doi: 10.1016/j.proeng.2012.09.522.
- [20] M. M. EL Gowini and W. Moussa, "A Finite Element Model of a MEMS-based Surface Acoustic Wave Hydrogen Sensor," *Sensors*, vol. 10, no. 2, pp. 1232–1250, Feb. 2010, doi: 10.3390/s100201232.
- [21] M. H. Tran, V. T. Trinh, T. T. Nguyen, and H. H. Si, "Modeling the selectivity of SAW filter with single phase unidirectional




- transducer based on FEM and equivalent circuit model,” *Measurement, Control, and Automation*, vol. 2, no. 1, 2021.
- [22] H. Chambon, P. Nicolay, G. Bruckner, and A. Benjeddou, “Analysis of the sensitivity to pressure and temperature of a membrane based SAW sensor,” *International Journal of Smart and Nano Materials*, vol. 8, no. 2–3, pp. 95–109, Jul. 2017, doi: 10.1080/19475411.2017.1335658.
- [23] J. C. A. Ondo, E. J. J. Blampain, G. N. Mbourou, S. Mc Murtry, S. Hage-Ali, and O. Elmazria, “FEM Modeling of the Temperature Influence on the Performance of SAW Sensors Operating at GigaHertz Frequency Range and at High Temperature Up to 500 °C,” *Sensors*, vol. 20, no. 15, Jul. 2020, doi: 10.3390/s20154166.
- [24] B. A. Auld, *Acoustic Fields and Waves in Solids*, 2nd Edition. Malabar: Krieger Publishing Company.
- [25] T. Kannan, “Finite element analysis of surface acoustic wave resonators,” University of Saskatchewan, 2006. [Online]. Available: <http://hdl.handle.net/10388/etd-07022006-160413>
- [26] D. R. and E. Dieulesaint, *Elastic waves in solids*. Berlin, New York: Springer, 2000.
- [27] D. Royer and E. Dieulesaint, “Rayleigh wave velocity and displacement in orthorhombic, tetragonal, hexagonal, and cubic crystals,” *The Journal of the Acoustical Society of America*, vol. 76, no. 5, pp. 1438–1444, Nov. 1984, doi: 10.1121/1.391427.
- [28] A. Massaro, R. Cingolani, and A. Passaseo, “3D fem modeling and technology of piezo-electric ring mems antenna,” *Progress In Electromagnetics Research C*, vol. 23, pp. 123–135, 2011, doi: 10.2528/PIERC11063003.
- [29] H. Trang *et al.*, “Trade-Off between Issues in AlN/SiO₂/Si Pressure Sensor,” in *2007 International Conference on Perspective Technologies and Methods in MEMS Design*, IEEE, May 2007, pp. 142–147, doi: 10.1109/MEMSTECH.2007.4283449.
- [30] R. K. Pati, S. K. M. Ali, S. Mohapatra, and M. Panigrahi, “Surface acoustics wave sensor by using piezoelectric devices,” in *Proceedings of the 2013 COMSOL Conference, Bangalore*, 2013, pp. 1–30. [Online]. Available: https://www.comsol.com/paper/download/183029/saw_paper.pdf
- [31] C. Caliendo, E. Verona, and V. I. Anisimkin, “Surface acoustic wave humidity sensors: a comparison between different types of sensitive membrane,” *Smart Materials and Structures*, vol. 6, no. 6, pp. 707–715, Dec. 1997, doi: 10.1088/0964-1726/6/6/007.

BIOGRAPHIES OF AUTHORS






Do Duy Phu    received his B.E and M.E degree at Hanoi University of Science and Technology, Hanoi, Vietnam, in 2001 and 2003, respectively. Now, he is a lecturer at the Faculty of Electrical Engineering, Hanoi University of Industry, Hanoi, Vietnam and studying as a Ph.D. student at the School of Electrical and Electronic Engineering, Hanoi University of Science and Technology, Vietnam. His research interests include piezoelectric material, SAW sensor, passive wireless sensor, and measurement and control. He can be contacted at email: doduyphu@hau.edu.vn.



Hoang Si Hong    received his B.E and M.E degree at the School of Electrical and Electronic Engineering from Hanoi University of Science and Technology, Hanoi, Vietnam, in 1999 and 2001, respectively, and his Ph.D. degree from the University of Ulsan, Ulsan, Korea, in 2010. Now, he is an associate professor at the School of Electrical and Electronic Engineering, Hanoi University of Science and Technology, Hanoi, Vietnam. His research interests include piezoelectric material, SAW sensor, passive wireless sensor, and harvesting energy. He can be contacted at email: hong.hoangsy@hust.edu.vn.



Le Van Vinh    received B.E degree in Engineering Physics, Hanoi University of Technology, Hanoi, Vietnam, Master of Science in Semiconductor Science and Technology, Jeonbuk National University, Korea, and Ph.D. degree from the University of Ulsan, Ulsan, Korea. Currently, he is an associate professor at the Faculty of Computer Science, Phenikaa University, Hanoi, Vietnam. His research interests are computational physics, materials modeling and design, and machine learning in materials modeling and design. He can be contacted at email: vinh.levan@phenikaa-uni.edu.vn.